

## Article

# A Machine Learning Approach to Predict Fluid Viscosity Based on Droplet Dynamics Features

Zhipeng Qin \*, Fulei Wang, Shengchang Tang and Shaohao Liang

School of Mechanical Engineering, Guangxi University, Nanning 530004, China; 2111392021@st.gxu.edu.cn (F.W.); shengchangtang@st.gxu.edu.cn (S.T.)

\* Correspondence: zhipengq@gxu.edu.cn

**Abstract:** In recent years, machine learning has made significant progress in the field of micro-fluids, and viscosity prediction has become one of the hotspots of research. Due to the specificity of the application direction, the input datasets required for machine learning models are diverse, which limits the generalisation ability of the models. This paper starts by analysing the most obvious kinetic feature induced by viscosity during flow—the variation in droplet neck contraction with time ( $h_{min}/R \sim \tau$ ). The kinetic processes of aqueous glycerol solutions of different viscosities when dropped in air were investigated by high-speed camera experiments, and the kinetic characteristics of the contraction of the liquid neck during droplet falling were extracted, using the Ohnesorge number ( $Oh = \mu/(\rho R\sigma)^{1/2}$ ) to represent the change in viscosity. Subsequently, the liquid neck contraction data were used as the original dataset, and three models, namely, random forest, multiple linear regression, and neural network, were used for training. The final results showed superior results for all three models, with the multivariate linear regression model having the best predictive ability with a correlation coefficient  $R^2$  of 0.98.

**Keywords:** droplet dynamics; neck of the liquid filament; machine learning; viscosity prediction



**Citation:** Qin, Z.; Wang, F.; Tang, S.; Liang, S. A Machine Learning Approach to Predict Fluid Viscosity Based on Droplet Dynamics Features. *Appl. Sci.* **2024**, *14*, 3537. <https://doi.org/10.3390/app14093537>

Academic Editor: Francesca Scargiali

Received: 13 March 2024

Revised: 27 March 2024

Accepted: 15 April 2024

Published: 23 April 2024



**Copyright:** © 2024 by the authors. Licensee MDPI, Basel, Switzerland. This article is an open access article distributed under the terms and conditions of the Creative Commons Attribution (CC BY) license (<https://creativecommons.org/licenses/by/4.0/>).

## 1. Introduction

The study of the rupture dynamics of Newtonian fluids was first started in 1870 by Plateau and Rayleigh [1,2]. It has been extensively developed over the last hundred years. The phenomenon of fluid frequently flows out from capillary tubes in various industrial and natural environments [3,4]. Due to the universality and importance of the free interfacial evolution process of liquid droplets, it has attracted the attention of many researchers. With the rapid development of computer technology, machine learning has demonstrated powerful data analysis capabilities, which have made great contributions to the development of many industries. Droplets of different sizes, physical properties, and concentrations are produced in processes involving droplet generation, such as micro-fluid [5,6], ink-jet printing [7], and spraying [8]. The study of droplet dynamics will generate a large number of valuable but complex droplet datasets. In the field of micro-fluid generation, engineers can optimise the composition and concentration of micro-fluid by accurately predicting the viscosity of the micro-fluid to maximise the accuracy of droplet generation [9]. Analyzing these complex data is beneficial for detecting and quantifying droplet generation, and machine learning tools have successfully demonstrated their capabilities in automating the most complex systems [10].

Despite the currently rich results at the intersection of droplet generation and machine learning, the generalisation of methods is still problematic because different models require different sets of raw data [11]. Flow rate, viscosity, surface tension, as well as geometrical parameters of droplet generation (width, length, height, angle), and kinetic parameters (pressure, frequency) all affect droplet generation. The multitude of reasons affecting droplet generation is the main reason for the inconsistency of the inputs to the datasets currently

used in viscosity studies. Meybodi et al. [12] used temperature, micro-particle, size and concentration to train a viscosity prediction model and used these data as raw inputs to predict the viscosity of a fluid containing micro-particles. Gholizadeh et al. [13] built on Meybodi's [12] study by adding micro-particle density and base fluid viscosity as inputs to the original dataset. Gholizadeh et al. found in the results that micro-particle concentration and base fluid viscosity had the greatest impact on the predicted results. Cengiz et al. [14] used the water content and density of the fluid as input data when predicting fuel viscosity.

These studies have used factors affecting mobility as the original inputs to the model, which is the main reason that limits the ability of the model to generalise. When the experimental equipment or fluid materials are different, the raw datasets are naturally different. In fact, when the viscosity of the fluid is different, each viscosity will exhibit different flow states due to different resistance to flow. In many problems where the viscosity has to be tested, there will be differences in the flow conditions due to the different viscosities. The ability to generalise the model would be greatly improved if the flow had a direct correlation with the viscosity based on the differences in flow characteristics. Therefore, it becomes important to understand droplet dynamics and to use more correlated datasets of flow characteristics.

The flow regimes during droplet generation are usually classified into three modes based on the size of the Weber number: three periodic dripping (PD), dripping faucet (DF), and jetting (J). In PD mode, droplets suspended at the nozzle outlet will fall due to gravity when the force of gravity exceeds the capillary force of the droplet. This mode is commonly used by researchers to study the evolution of the drop process and the contraction of the liquid neck due to the stable and reproducible results of the droplet falling and contraction process [15,16]. It has been shown that the three physical parameters that play a major role in the PD drop pattern of Newtonian fluids are viscosity  $\eta$ , surface tension  $\sigma$ , and inertia. The dimensionless numbers used to quantify the process are the Ohnesorge number ( $Oh = \mu/(\rho R\sigma)^{1/2}$ ), Bond number ( $Bo = (\rho g R^2)/\sigma$ ), and Weber number ( $We = \rho U^2 R/\sigma$ ). Of these, surface tension is responsible for minimising the surface area of the fluid, giving it a spherical shape while viscous forces impede and slow down the flow of the fluid. Three theories have been developed to describe the kinetic behaviour of liquid neck contraction during capillary drop [16–22]. When the viscosity of the fluid is negligible, the liquid neck thickness changes exponentially concerning time  $h_{min}/R \sim \tau^{2/3}$ , and inertia plays a major role in the contraction (I—inertia regime).  $\tau$  is the remaining time before pinch-off dimensionless.  $R$  denotes the outer radius of the needle, and the  $h_{min}$  denotes half of the fluid neck thickness dimension. When the inertia of the fluid is negligible, the contraction of the neck thickness follows the following scalar law  $h_{min}/R = (0.0709/Oh)\tau$ . When the Reynolds number of the fluid is very small, viscosity plays a major role, showing the characteristics of Stokes flow (V—viscous regime). When both viscosity and inertia are not negligible, the change in the thickness of the liquid neck follows the following scalar law  $h_{min}/R = (0.0304/Oh)\tau$  or  $h_{min} \sim \tau^{1/2}$ , viscosity, and inertia in the process of joint action of the liquid filament contraction fracture (IV—inertial viscous regime).

The neck contraction process showed consistency under other complex influencing factors, which suggests that the results of neck contraction can be generalised to similar flow situations. Huang et al. [21] investigated in detail the neck stretching and fracture process of droplets separated by collision. The results of this study showed that the neck contraction and fracture process of droplets bouncing and separating after the collision is consistent with the scalar law of the drop as it falls. Poulouze et al. [23] investigated the neck shrinkage kinetics of paramagnetic solutions in a magnetic field environment. Wang et al. [24] and Rubio et al. [25] investigated the droplet dropping and liquid bridge stretching in an electric field environment, respectively. Vagner et al. [26] investigated the generation process of micro-droplets in a double-layer pipeline. Liu et al. [27] investigated the neck shrinkage kinetics of the droplet dropping on the surface of a horizontal pipeline. All these studies have shown that the necking contraction process that occurs during

droplet formation, despite the presence of other influencing factors, is usually affected by the changes in the surface tension, viscosity, and inertia due to the influence of the three, thus altering the competing relationship between these three factors.

Previously, the effect of low viscosity ( $Oh < 0.001$ ), medium viscosity ( $1 > Oh > 0.001$ ), and high viscosity ( $Oh > 1$ ) on the contraction of the liquid neck has been elucidated. Jiang et al. [22] studied the effect of viscosity ratio on fluid flow and found that at relatively high viscosities ( $6.3 \times 10^3$  and  $3.3 \times 10^3$ ), the contraction region in the neck of the fluid shows an I–V–IV transition. Whereas, an I–V shift in the contraction region was observed for droplets with lower viscosities ( $6.4 \times 10^2$ ). Jiang et al. judged the contraction regime based on the exponential size of the contraction curve, with an exponent of  $2/3$  being the inertial regime (I), and an exponent of 1 being the viscous regime (V) as well as the viscous–inertial regime (IV). Similar to the way other researchers judge changes in contraction regions [23,28–31], their judgments of V and IV tenses are based on two non-overlapping, exponentially 1 contractions.

In this paper, we use the same judgment as Castrejón-Pita et al. [16] and Wee et al. [19] to demonstrate the transition of regime V (viscous regime) by the coincidence of specific equations with experimental data. In drop experiments with aqueous glycerol solutions of different viscosities, the contraction curves of the liquid necks are different due to the viscosity, resulting in different stages of contraction experienced, producing different contraction curves. The viscosity of each glycerol aqueous solution corresponds to a contraction curve. Liquid neck shrinkage data can be learned by machine learning models as it correlates more strongly with viscosity, thus predicting the viscosity of aqueous glycerol solutions. The use of dimensionless data as input makes the model more generalisable. Subsequently, three models, namely random forest, multiple linear regression, and neural network, were used to train the liquid neck contraction data and compare the prediction results with the actual values, and all three models showed good prediction results.

## 2. Materials and Methods

The dataset for this paper comes from a self-designed experiment. The experimental setup is shown in Figure 1. A precision flow pump (ELITE PICO SINGLE, Harvard Apparatus, Los Angeles, CA, USA) was used for fluid administration, and the flow rate  $Q$  was set to  $Q = 0.2$  mL/min. The needle was fixed to the acrylic plate through a luer connector, the acrylic plate was fixed to a stand through a threaded peg, and the needle was adjusted to level by adjusting the threaded pegs with a level. Droplet images were captured using a high-speed video camera (FASTCAM MINI UX100 TYPE 200K-M, Photron, Tokyo, Japan) with a 100 mm fixed-focus lens (AT-X 24-70 F2.8 PRO FX, TOKINA, Tokyo, Japan). The camera was set to a shooting speed of 4000 fps, a shutter speed of  $1/10,000$  s, a resolution of  $1280 \times 1024$ , and a pixel ratio of  $13.7 \mu\text{m}/\text{pixel}$ . A strobe-less LED light source (CDXINT XT120W, CDXINT, Chengdu, China) was used to fill in the light during shooting. To obtain smaller-scale changes in the filament, a homogeneous PMMA plate was used to shade the LED light source, reducing the amount of incoming light while maintaining the shutter speed, and reducing the diffraction of light so that the fine fluid details of the filament breakage could be shown. The needle material used was 304 steel, and the outer radius of the needle was  $R = 0.8$  mm. A self-programmed ImageJ v.1.53t script program was used to capture the characteristic dimensions of the neck thickness during the dropping process.

This study focuses on the kinetic characteristics of the viscosity of aqueous glycerol solutions during the dropping process, capturing the drop neck contraction data that have the strongest correlation with viscosity for use in training a machine learning model to establish a direct relationship between neck contraction and viscosity. Glycerol–water solutions can be prepared at varying percentages by adjusting the concentration of glycerol, allowing for the easy acquisition of fluid samples with different concentrations. Additionally, the influence of glycerol's viscosity on surface tension and density is minimal, which is advantageous for comparing experimental results related to viscosity differences. The commonality of glycerol–water solutions as standard samples enables convenient comparison

and validation with other experimental outcomes, thereby promoting the reliability and accuracy of experimental results.

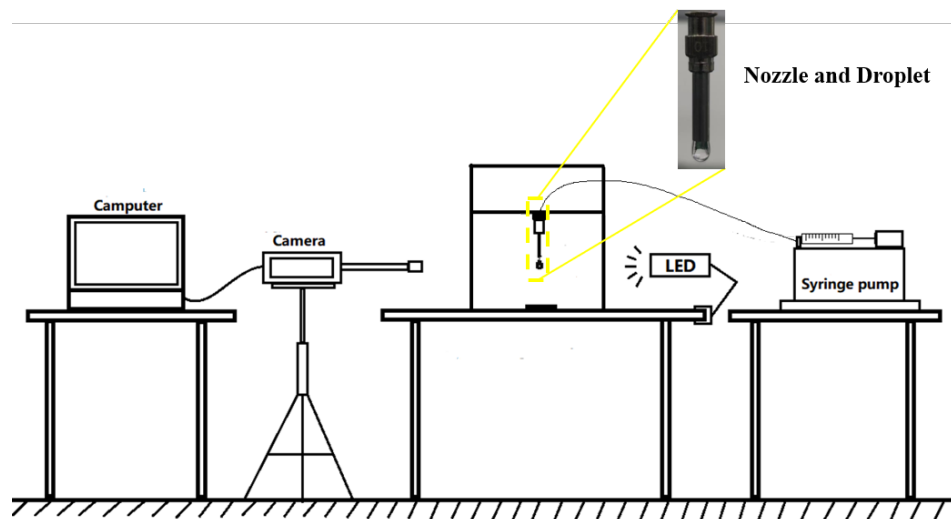


**Figure 1.** Scheme of the experimental setup. The device was made using an aluminum stand surrounded by a transparent 0.1 mm PMMA sheet, with the needle fixed in the centre of the device and levelled using a spirit level for generating stable droplets.

We then enabled the input of drop video data of unknown viscosity to predict the viscosity of that fluid. In this work, first, eleven aqueous solutions of glycerol with different percentages were formulated; the concentrations of the glycerol aqueous solutions were distributed from 50% to 99% at 5% intervals and the physical parameters of different percentages of glycerol aqueous solutions are shown in Table 1. Due to the existence of humidity, temperature, and other error factors, even if the same glycerol aqueous solution is used in the experiments conducted at different times, there will be some errors. For the accuracy of the liquid neck shrinkage–viscosity dataset, the viscosity of the solution was measured once before each experiment, and the first drop video data of each viscosity counterpart was measured for that solution. Finally, eighteen liquid neck shrinkage–viscosity datasets were collected. The Greek letters  $\rho$ ,  $\mu$ , and  $\sigma$  denote density, surface tension, and viscosity, respectively. Eggers et al. [20] proposed that the free surface shape and the internal flow of a droplet depend only on the proportionality of the observed scale to the viscous scale. The viscous scale  $l_\mu = \mu^2 / (\sigma\rho)$  indicates that the viscous effect increases significantly when the flow scale of the fluid reaches this scale.

**Table 1.** Physical properties of glycerol aqueous solution 25 °C.

Property	$\rho/(\text{kg/m}^3)$	$\sigma/(\text{mN/m})$	$\mu/(\text{mPa}\cdot\text{s})$	$l_\mu/(\mu\text{m})$
50% glycerol–water	1200	70.5	6.1	0.44
55% glycerol–water	1200	70.4	8.5	0.86
60% glycerol–water	1205	70.1	10.5	1.31
65% glycerol–water	1210	70.1	15.2	2.72
70% glycerol–water	1215	70.0	41.2	19.96
75% glycerol–water	1220	69.9	67.1	52.79
80% glycerol–water	1230	69.7	97.1	109.98
85% glycerol–water	1240	69.5	126.3	185.10
90% glycerol–water	1250	69.3	208.5	501.84
95% glycerol–water	1255	69.3	394.8	1792.16
99% glycerol–water	1265	69.1	824.2	7802.19

Three machine learning models based on multivariate linear regression, random forest, and neural network were used in this study to model the obtained fluid neck contraction dataset. A homebrew program was written in Python using scikit-learn, a widely used open-source machine learning library for Python, often abbreviated to learn [31]. Scikit-learn provides various preprocessing methods including data scaling, normalisation, categorical variable coding, dealing with missing values, and feature extraction. These methods play an important role before using the data in machine learning models [32].

Multiple linear regression is a statistical technique used to predict the relationship between a dependent variable and one or more independent variables, based on the assumption of a linear relationship between the independent and dependent variables. The algorithm used in this paper is the least squares method, which fits the model parameters by minimising the sum of squared residuals (RSS), which also serves as the loss function of this model. Here,  $y_i$  represents the true value of sample  $i$ , and  $\hat{y}_i$  is the predicted result. The sum of squared residuals is given by Equation (1).

$$RSS = \sum_{i=1}^m (y_i - \hat{y}_i)^2 \quad (1)$$

Random forest is an integrated learning method consisting of multiple decision trees. Each decision tree is constructed based on a randomly selected subset of features and training samples with put-back sampling. This introduction of randomness makes random forest highly diverse and generalisable. In the random forest algorithm, the generalisation error is given and the formula is given by Equation (2) [33], where the subscripts ( $X$ ) and ( $Y$ ) are random vectors indicating that the probability is on the space ( $X$ ), ( $Y$ ), and ( $mg$ ) is the bounding function.

$$PE = P_{X,Y}(mg(X,Y) < 0) \quad (2)$$

A neural network is a model of a machine learning algorithm that is inspired by the network of neurons in the human brain. A neural network consists of multiple layers of neurons, each of which receives inputs from the previous layer of neurons and processes these inputs with weights and activation functions to finally produce an output. The basic computational formula can be expressed as Equation (3) [34].

$$y = f(x, \{W_i\}) + x, \quad (3)$$

where  $y$  denotes the output of the neuron;  $f$  is the activation function, which introduces non-linear characteristics;  $W_i$  denotes the weight, which indicates the importance of the input; and  $x$  is the input vector.

### 3. Results and Discussion

Figure 2a represents the detailed process of a droplet falling for  $Oh = 0.15$  (70% G-W) and  $Bo = 0.108$  ( $R = 0.8$  mm). To study the kinetics of the contraction process of the liquid neck, a dimensionless analysis was used.  $h_{min}$  represents the outer radius of the liquid neck and  $R$  is the outer radius of the needle.  $\tau$  represents the dimensionlessness of the remaining time before the liquid neck breaks  $\tau = (t_b - t)/t_{cap}$ ,  $t_{cap}$  is the capillary time,  $t_{cap} = (\rho R^3/\sigma)^{1/2}$ ,  $t_b$  is the time at the moment of the break, and  $t$  is the real time.

The liquid neck pinch-off process is shown in Figure 2b. As the droplet is detached from the needle, the curvature at the liquid neck increases, the effect of surface tension is gradually enhanced, and the contraction process is accelerated, eventually forming a strip of liquid filament, with fracture occurring at the thinnest point. Due to the different curvature of the two sides, the process of contraction of the two sides of the liquid filament is also different. The liquid filament close to the side of the liquid sphere is faster to break, because the curvature change here is more intense, and the effect of surface tension is more obvious. The difference between the two sides of the liquid neck contraction can be observed in Figure 2c, which becomes apparent in the later stage of the contraction.

Approximately 1.25 ms after the pinch-off (indicated by the blue line), the curvature of the two sides begins to change. The liquid filament gradually elongates, and two possible locations of fracture, one upper and one lower, start to appear. As the droplets fall off, the process is illustrated by the green, red, and black lines, where the curvature on the lower side exceeds that on the upper side. Eventually, the lower side, with the greater curvature, undergoes fracture first.

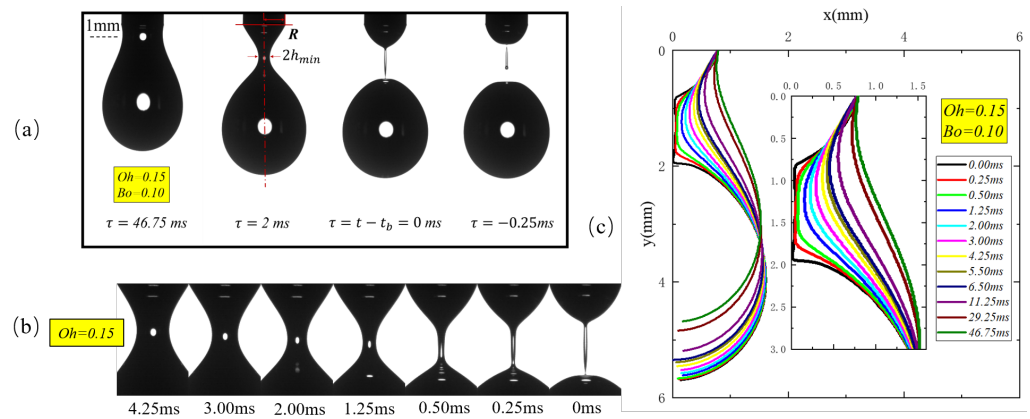


**Figure 2.** Definition of  $h_{min}$  and  $R$  ( $Bo = 0.10$  and  $Oh = 0.15$ ). (a)  $h_{min}$  and  $R$  definition; (b) contraction process of the local liquid neck of the drop; (c) evolution of the outer contour of the drop process.

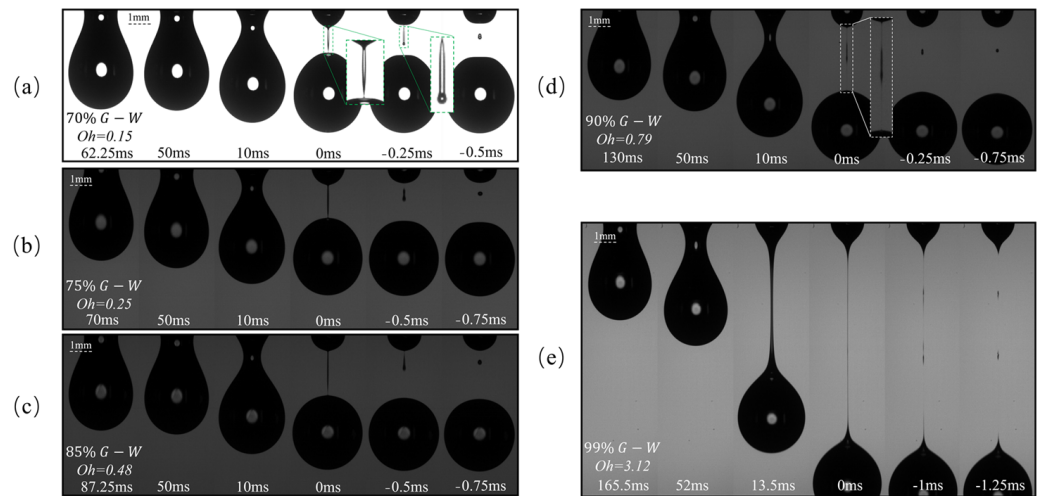
### 3.1. Droplet Dynamics Analysis

Figure 3 shows drop experiments with five different viscosities of glycerol–water (G–W) solutions of 70%, 75%, 85%, 90%, and 99%, exploring the drop process induced by gravity. For the lower viscosity  $Oh = 0.15$ ,  $Oh = 0.25$ , and  $Oh = 0.48$  fluids, as shown in Figure 3a–c, as the flow pump slowly pushes in the fluid, the droplet begins to accelerate away from the needle when the gravity of the droplet exceeds the surface tension. At this point there is the appearance  $h_{min} < R$  of the liquid neck, and the length of the droplet increases, the thickness of the droplet  $h_{min}$  decreases rapidly, and then, as shown in the small dashed line in Figure 3a at the moment of 0 ms, the liquid neck appears asymmetric and inhomogeneous at the upper and lower ends, and an END-PINCHING fracture occurs [18]. As the lower end breaks, shrinkage occurs first; when the upper end breaks, the resulting independent liquid filaments have undergone shrinkage at the lower end, manifesting as a rounded sphere, and the upper side manifests as a sharp cone when it just breaks, as shown in the small green dashed line in Figure 3a at  $-0.25$  ms. For the higher viscosity  $Oh = 0.79$  versus  $Oh = 3.12$  G–W solutions, the droplets fall more slowly, the viscosity impedes fluid flow, fluid flow inside the liquid neck is more difficult, the droplets fall further, and the liquid filaments are stretched longer.

Figure 4 demonstrates that as the time before pinch-off decreases, the liquid neck thickness  $h_{min}$  decreases. In Figure 4a, the neck thickness decreases as the time from pinch-off decreases, and the neck thickness decreases faster and faster as the time decreases. It can be seen that it takes more time for the droplet with higher viscosity to clamp off because the viscosity of the fluid hinders the flow of the fluid, the flow inside the neck is inhibited, and it is more difficult for the fluid to flow outward from the neck, which slows down the contraction of the neck.

Figure 4b shows  $h_{min}/R = (0.0709/Oh)\tau + a$  against the experimental data curve. The constant  $a$  ( $h_{min}/R = (0.0709/Oh)\tau + a$ ) was increased to correct the overlap with the experimental data. In the study of Castrejón-Pita et al. [16], the correction constants for the viscous regime corresponding to  $Oh = 0.23$  are  $-0.005$ ,  $a$  is  $0.03$  for  $Oh = 0.55$ , and  $a$  is  $0.33$  for  $Oh = 1.81$ . In our experiments, the similar viscosities and the correction constants correspond to, respectively,  $-0.02$  for  $Oh = 0.25$ ,  $a$  is  $0.03$  for  $Oh = 0.79$ , and  $a$  of  $0.25$  for  $Oh = 3.12$ . The slight difference with the Castrejón-Pita results is a negligible error in the mapping process. In this regime, viscosity is the main action in the contraction regime.

When the contraction process shifts from the inertial to the viscous regime, there exists a transient that makes the inertial, viscous action balanced [35], and usually the transition occurs at  $h_{min}/R \sim Oh^2$  [20,35]. The dashed line in Figure 4b represents  $h_{min}/R \sim Oh^2$  the position of this critical value in the longitudinal coordinate, and the colour of the dashed line for the same viscosity is the same as that of the liquid neck contraction line. For example, when  $Oh = 0.79$ , the horizontal light blue dashed line represents the  $h_{min}/R \sim Oh^2$  size and the light blue dashed line intersects with the light blue neck shrinkage line, which indicates that the effect of stickiness increases and affects the shrinkage process after the neck has theoretically shrunk to this size threshold. The theoretical transition thresholds of  $Oh = 0.15$ ,  $Oh = 0.25$ ,  $Oh = 0.48$ , and  $Oh = 0.7$  are marked in the figure  $h_{min}/R \sim Oh^2$ . The theoretical value is closest to the experimental value in the case of  $Oh = 0.79$ . As the number of  $Oh$  increases, the experiment shows the same trend as the theory.



**Figure 3.** Sequence of different viscosity fluids dripping in the air from the same needle ( $R = 0.8$  mm,  $Q = 0.2$  mL/min). All images in the figure share the scale. (a)  $Oh = 0.18$ ; (b)  $Oh = 0.25$ ; (c)  $Oh = 0.48$ ; (d)  $Oh = 0.79$ ; (e)  $Oh = 3.12$ .

Figure 4c illustrates the regime of inertial–viscous contraction in the final stage of contraction of G–W liquid necks for five viscosities. The combined effect of viscosity and inertia in this contraction regime leads to the fracture of the liquid neck. The critical  $h_{min}$  for the emergence of this regime was shown to vary with  $Oh$  in Castrejón-Pita’s study, with smaller  $Oh$  numbers leading to smaller  $h_{min}$ . When  $Oh = 0.23$ , the emergence of regime IV was found to be at  $h_{min} = 0.01$ , and the experimental results can be seen in Figure 4c.

Figure 4d illustrates the evolution of the liquid neck contraction state during the droplet falling process. When  $Oh = 0.15$  to  $0.79$ , the contraction of the liquid neck is initially dominated by inertia (regime I—*inertia*), then the influence of viscosity gradually increases (regime V—*viscosity*), and ultimately rupture occurs under the combined action of viscosity and inertia (regime IV—*viscosity–inertia*). For the 99% G–W solution, when  $Oh > 1$ , the hindrance of viscosity to flow starts earlier and is manifested in the initial stage of liquid neck contraction, followed by entry into the inertia contraction region with an exponent of  $2/3$  (regime I—*inertia*). The contraction process is characterised by a transition from regime V to regime I, ultimately leading to rupture under the combined effects of viscosity and inertia (regime IV—*viscosity–inertia*). However, in the study by Castrejón-Pita, the range of action of the inertia region (regime I) is within the interval where  $h_{min}/R$  is greater than  $10^{-2}$  and less than  $10^{-1}$ . In our study, the action range of the inertia region (regime I) is around  $10^1$ . Furthermore, in the experimental data, it is observed that there is a region with a contraction exponent of  $3/2$  between the inertia region (regime I) and the viscosity region (regime IV) during the liquid neck contraction process when  $Oh > 0.48$ , as indicated by the black line in Figure 4d. Broboana et al. [29] referred to this as the transitory regime (TR). In the article by Castrejón-Pita et al. [16], experimental data at  $Oh = 1.81$  also show a contraction process

with an exponent greater than 1 following the inertia region (regime I), a phenomenon commonly observed in other experimental studies [21,23,27,28,30]. However, there is currently no comprehensive theoretical explanation for this contraction process.

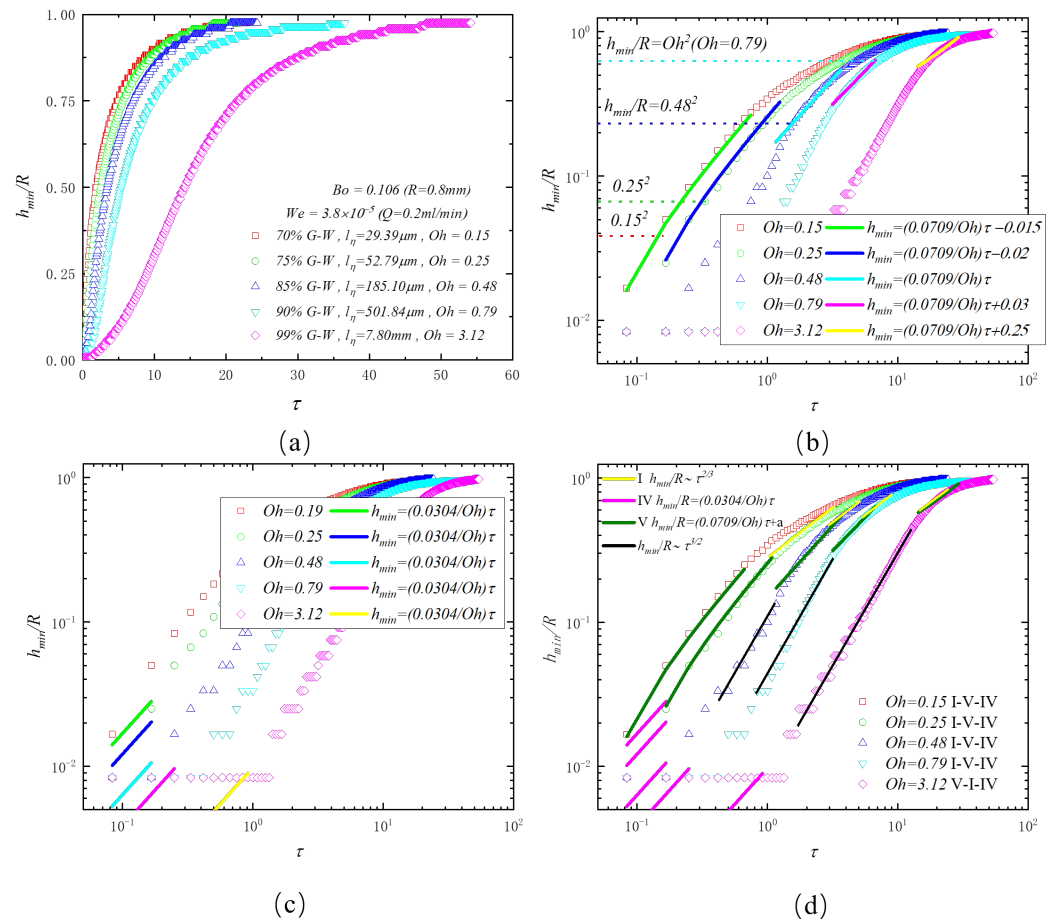


**Figure 4.** Scaling law of liquid neck contraction. (a) Thickness of liquid neck  $h_{min}$  with time  $\tau$  change. (b) Regime V (viscous contraction regime)  $h_{min}/R = (0.0709/Oh)\tau$  [9] comparison of theoretical viscous contraction curves (solid line) with experimental data (data points), the dashed line indicates the critical threshold at the beginning of the vicious contraction in the theoretical regime V  $h_{min}/R$  values. Each viscosity corresponds to a theoretical critical change value from regime I to regime V, and the dashed line is coloured the same as the corresponding viscosity. The theoretical critical value ( $h_{min}/R$ ) of  $Oh = 3.12$  is much larger than 1, indicating that the droplet is initially in the viscous contraction region at the very beginning of the drop, with viscosity playing a major role. (c) The extent to which the viscous–inertial regime plays a major role in the contraction process. (d) The regime division of the whole process of contraction of the liquid neck.

### 3.2. Viscosity Prediction from Liquid Neck Data

Droplet dynamics was investigated in Section 1. The reduction process of the neck thickness  $h_{min}/R$  is mainly affected by viscosity, inertia, and surface tension, and the contraction regime during neck contraction changes when the viscosity of glycerol aqueous solution varies. In this section, random forest, neural network, and multiple linear regression are used to predict the viscosity based on the contraction curve data of the neck thickness  $h_{min}/R$  for the variation in the neck contraction curve with viscosity.

Eleven different percentages of aqueous glycerol solutions were used in the experiments, and due to errors, 18 sets of data for the viscosity–droplet neck contraction curves were finally obtained, and the data can be seen in Figure 5. Each shrinkage curve has about 400 data points, totaling  $18 \times 400$  total data. The raw dataset was obtained by measuring the variation of liquid neck thickness frame by frame using a self-programmed program

after capturing the video of the drop with a high-speed camera. The dataset was divided into training and test sets according to a 1:1 ratio, with nine curves used as the training set and nine as the test set. As can be seen in Figure 5, the thickness of the liquid neck increases with the increase in the dataset. The vertical coordinate is  $h_{min}/R$  and the horizontal coordinate is the number of data points. A uniform FPS was used for shooting to ensure that the time interval of each image was kept consistent to avoid compression or elongation of the curves when the number of data points was used as the horizontal coordinate.

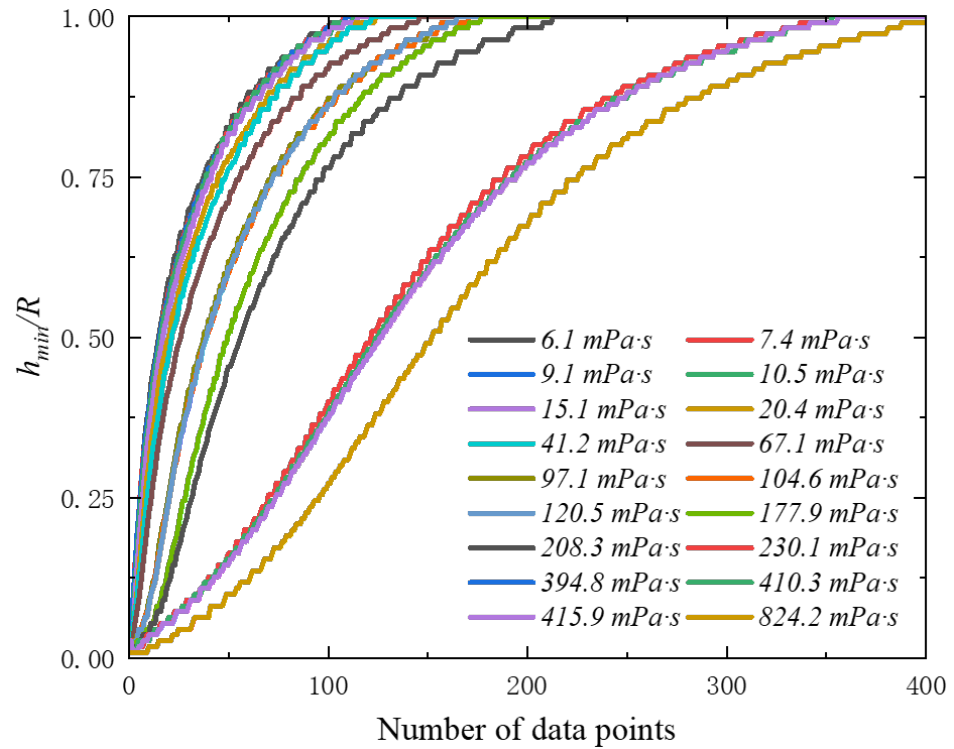


**Figure 5.** Plot of 18 sets of viscosity–neck curve data, with  $h_{min}/R$  indicating the ratio of liquid neck thickness to needle radius in the vertical coordinate and the number of data points in the horizontal coordinate.

The liquid neck shrinkage data used were dimensionless and all values lie between 0 and 1, so no normalisation was required. For the low-viscosity aqueous glycerol solution, due to the faster dropping time than the high-viscosity one, there will be missing values after the value of the data point reaches 1, and all of them will be made up with 1. There are several adjustable parameters in every machine learning model. However, finding the optimal combination of parameters is time-consuming and beyond the scope of the current research. As this work focusses on feature selection of the data, only the most important parameters were optimised, and the parameter settings for the three models can be seen in Tables 2–4. All other unlabelled parameters are default values.

**Table 2.** List of important parameters of random forest.

Parameters	Max Depth	Min Samples Split	Min Samples Leaf	Number of Trees
Random Forest	30	2	1	200

**Table 3.** List of important parameters of multiple linear regression.

Parameters	Copy	Max Iter	N-Components	Scale
Multiple Linear Regression	True	100	10	False

**Table 4.** List of important parameters of the neural network.

Parameters	Hidden Layer Sizes	Activation	Solver	Max Iter
Neural Network	(200, 100, 50)	Relu	Adam	2000

We used  $R^2$ , MAE, RMSE, and plots of true versus predicted values to assess the accuracies of the models [36]. The values for the three models can be seen in Table 5. The coefficient of determination ( $R^2$ ) is an important parameter in assessing the performance of a regression model. Its definition is shown in Equation (4).

$$R^2 = 1 - \frac{(\text{Actual}_i - \text{Predicted}_i)^2}{(\text{Actual}_i - \text{mean of the observer data}^2)} \tag{4}$$

It determines how close the predicted data values are to the regression line. If the  $R^2$  value tends to 1, it means that the regression model is perfect, and if  $R^2$  is 0, it means that the regression model is a complete failure, i.e., no variance is explained by the regression. The multiple linear regression model has the best coefficient of determination with  $R^2 = 0.98$ , followed by the neural network with  $R^2 = 0.97$ , and the random forest performs relatively well with  $R^2 = 0.95$ .

**Table 5.** Performance of the model.

	Multiple Linear Regression	Neural Network	Random Forest
$R^2$	0.98	0.97	0.95
MAE	13.85	14.29	18.55
RMSE	16.95	19.65	25.14

For the regression model, MAE is used to measure the average absolute difference between predicted and actual values. Equation (5) is used to calculate the MAE value, where  $Actual_i$  is the actual value,  $Predicted_i$  is the predicted value, and N is the total number of instances. The average error of the regression model is measured by RMSE. Equation (6) is used to calculate the RMSE. The magnitudes of both the MAE and RMSE values depend on the size of the predicted outcome and are used for comparison between multiple models of a dataset.

$$MAE = \frac{\sum_{i=1}^N | \text{Actual}_i - \text{Predicted}_i |}{N} \tag{5}$$

$$RMSE = \sqrt{\frac{\sum_{i=1}^N (\text{Actual}_i - \text{Predicted}_i)^2}{N}} \tag{6}$$

The  $R^2$ , MAE, and RMSE results for random forest, multiple linear regression, and neural networks are recorded in Table 5 for comparison. The best results for viscosity prediction are shown in the multiple linear regression model, which provided the smallest MAE and RMSE values of 12.85 and 16.95. Figure 6 shows the  $R^2$  values and fitted regression lines for the three models (random forest, multiple linear regression, and neural network). The vertical coordinate is the result of model prediction using the prediction set, the horizontal coordinate is the true viscosity of the prediction set, and the dashed line is the line of best results. The multivariate linear regression model has the closest  $R^2$  to 1, with the most accurate results, and it can also be seen in Table 5 that multivariate linear regression also has the smallest MAE and RMSE compared to random forests and neural networks. In our next work, we plan to continue to extract other kinetic data such as drop time, drop volume, and drop length to improve the accuracy of the model. We also plan to automate the data extraction and dimensionless process so that the predicted viscosity parameters can be output by inputting the video data only.

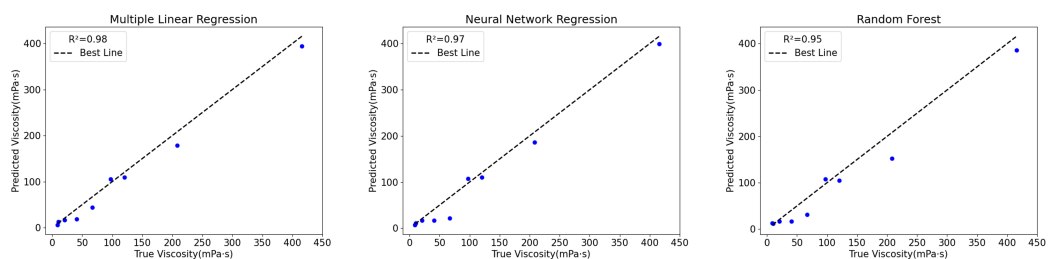


**Figure 6.** Plot of true-prediction results for multiple linear regression, random forest, neural network, and  $R^2$ .

#### 4. Conclusions

In this paper, we first conducted droplet experiments on glycerol aqueous solutions. Then we analysed the kinetic process of liquid neck contraction during droplet falling and discussed the strong correlation between viscosity and the contraction process. Subsequently, based on the experimentally demonstrated strong correlation between viscosity and the liquid neck contraction process, the relationship was established using a machine learning model with liquid neck contraction data as the dataset.

In the first part of the Section 3, the droplet neck contraction curves of the dropping process of five aqueous glycerol solutions with different viscosities were analysed and compared with other research results. The results show that viscosity has a great influence on the droplet neck contraction process. This was manifested by the change in the contraction curve. Based on the correlation between the droplet neck contraction process and viscosity, three machine learning models were used for modelling. After extracting the liquid neck contraction data through a self-programmed procedure, they were dimensionless and the factors related to specific scales were removed to be more general and universal. Three machine learning models, neural network, multiple linear regression and random forest, were used to train the model using the liquid neck contraction data and predict the viscosity of the fluid based on the contraction data. The results show that the three models using fluid neck contraction data are more effective, with random forest having the lowest correlation coefficient  $R^2$  of 0.95, while multiple linear regression gives more accurate predictions with a correlation coefficient  $R^2$  of 0.98, and multiple linear regression has the smallest  $MAE$  and  $RMSE$  among the three models, at 12.85 and 16.95.

**Author Contributions:** Conceptualisation, Z.Q.; methodology, F.W.; formal analysis, F.W. and S.T.; investigation, S.L.; resources, Z.Q.; data curation, Z.Q. and F.W.; writing—original draft preparation, S.L.; writing—review and editing, Z.Q., F.W. and S.T.; supervision, Z.Q.; project administration, F.W.; funding acquisition, Z.Q. All authors have read and agreed to the published version of the manuscript.

**Funding:** This study is supported by the National Natural Science Foundation of China (Grant No. 12172094) and Guangxi Bagui Scholars Project (No. 2019A02).

**Data Availability Statement:** Data are contained within the article.

**Conflicts of Interest:** The authors declare no conflicts of interest.

#### References

1. Plateau, J.I. Experimental and theoretical researches on the figures of equilibrium of a liquid mass withdrawn from the action of gravity.—Third series. *Lond. Edinb. Dublin Philos. Mag. J. Sci.* **1857**, *14*, 1–22. [[CrossRef](#)]
2. Rayleigh, L. On the instability of jets. *Proc. Lond. Math. Soc.* **1878**, *1*, 4–13. [[CrossRef](#)]
3. Gart, S.; Socha, J.J.; Vlachos, P.P.; Jung, S. Dogs lap using acceleration-driven open pumping. *Proc. Natl. Acad. Sci. USA* **2015**, *112*, 15798–15802. [[CrossRef](#)]
4. Reis, P.M.; Jung, S.; Aristoff, J.M.; Stocker, R. How cats lap: Water uptake by *Felis catus*. *Science* **2010**, *330*, 1231–1234. [[CrossRef](#)]
5. Whitesides, G.M. The origins and the future of microfluidics. *Nature* **2006**, *442*, 368–373. [[CrossRef](#)]
6. Sun, H.; Xie, W.; Mo, J.; Huang, Y.; Dong, H. Deep learning with microfluidics for on-chip droplet generation, control, and analysis. *Front. Bioeng. Biotechnol.* **2023**, *11*, 1208648. [[CrossRef](#)]
7. Basaran, O.A.; Gao, H.; Bhat, P.P. Nonstandard inkjets. *Annu. Rev. Fluid Mech.* **2013**, *45*, 85–113. [[CrossRef](#)]

8. Yaseen, M.; Khattak, M.A.K.; Khan, A.; Bibi, S.; Bououdina, M.; Usman, M.; Khan, N.A.; Pirzado, A.A.A.; Abumousa, R.A.; Humayun, M. State-of-the-art electrochromic thin films devices, fabrication techniques and applications: A review. *Nanocomposites* **2024**, *10*, 1–40. [[CrossRef](#)]
9. Ganga, S.; Uddin, Z.; Asthana, R.; Hassan, H.; Bhardwaj, A. Modelling of Viscosity and Thermal Conductivity of Water-Based Nanofluids using Machine-Learning Techniques. *Int. J. Math. Eng. Manag. Sci.* **2023**, *8*, 817. [[CrossRef](#)]
10. Das, S.; Dey, A.; Pal, A.; Roy, N. Applications of artificial intelligence in machine learning: Review and prospect. *Int. J. Comput. Appl.* **2015**, *115*, 31–41. [[CrossRef](#)]
11. LaBelle, C.A.; Massaro, A.; Cortés-Llanos, B.; Sims, C.E.; Allbritton, N.L. Image-based live cell sorting. *Trends Biotechnol.* **2021**, *39*, 613–623. [[CrossRef](#)]
12. Meybodi, M.K.; Naseri, S.; Shokrollahi, A.; Daryasafar, A. Prediction of viscosity of water-based Al<sub>2</sub>O<sub>3</sub>, TiO<sub>2</sub>, SiO<sub>2</sub>, and CuO nanofluids using a reliable approach. *Chemom. Intell. Lab. Syst.* **2015**, *149*, 60–69. [[CrossRef](#)]
13. Gholizadeh, M.; Jamei, M.; Ahmadianfar, I.; Pourrajab, R. Prediction of nanofluids viscosity using random forest (RF) approach. *Chemom. Intell. Lab. Syst.* **2020**, *201*, 104010. [[CrossRef](#)]
14. Cengiz, E.; Babagiray, M.; Aysal, F.E.; Aksoy, F. Kinematic viscosity estimation of fuel oil with comparison of machine learning methods. *Fuel* **2022**, *316*, 123422. [[CrossRef](#)]
15. Day, R.F.; Hinch, E.J.; Lister, J.R. Self-similar capillary pinch-off of an inviscid fluid. *Phys. Rev. Lett.* **1998**, *80*, 704. [[CrossRef](#)]
16. Castrejón-Pita, J.R.; Castrejón-Pita, A.A.; Thete, S.S.; Sambath, K.; Hutchings, I.M.; Hinch, J.; Lister, J.R.; Basaran, O.A. Plethora of transitions during breakup of liquid filaments. *Proc. Natl. Acad. Sci. USA* **2015**, *112*, 4582–4587. [[CrossRef](#)]
17. Anthony, C.R.; Wee, H.; Garg, V.; Thete, S.S.; Kamat, P.M.; Wagoner, B.W.; Wilkes, E.D.; Notz, P.K.; Chen, A.U.; Suryo, R.; et al. Sharp interface methods for simulation and analysis of free surface flows with singularities: Breakup and coalescence. *Annu. Rev. Fluid Mech.* **2023**, *55*, 707–747. [[CrossRef](#)]
18. Eggers, J. Nonlinear dynamics and breakup of free-surface flows. *Rev. Mod. Phys.* **1997**, *69*, 865. [[CrossRef](#)]
19. Wee, H.; Anthony, C.R.; Basaran, O.A. Breakup of a low-viscosity liquid thread. *Phys. Rev. Fluids* **2022**, *7*, L112001. [[CrossRef](#)]
20. Eggers, J. Drop formation—An overview. *ZAMM—Z. Angew. Math. Mech.* **2005**, *85*, 400–410. [[CrossRef](#)]
21. Huang, K.L.; Pan, K.L.; Josserand, C. Pinching dynamics and satellite droplet formation in symmetrical droplet collisions. *Phys. Rev. Lett.* **2019**, *123*, 234502. [[CrossRef](#)] [[PubMed](#)]
22. Jiang, X.; Xu, E.; Meng, X.; Li, H.Z. The effect of viscosity ratio on drop pinch-off dynamics in two-fluid flow. *J. Ind. Eng. Chem.* **2020**, *91*, 347–354. [[CrossRef](#)]
23. Poulouse, S.; Quirke, J.A.; Stamenov, P.; Möbius, M.E.; Coey, J. Deformation and necking of liquid droplets in a magnetic field. *Phys. Fluids* **2022**, *34*, 112116. [[CrossRef](#)]
24. Wang, Z.; Zhang, Y.; Wang, Q.; Dong, K.; Yang, S.; Jiang, Y.; Zheng, J.; Li, B.; Huo, Y.; Wang, X.; et al. Dynamics of droplet formation with oscillation of meniscus in electric periodic dripping regime. *Exp. Therm. Fluid Sci.* **2021**, *120*, 110250. [[CrossRef](#)]
25. Rubio, M.; Ponce-Torres, A.; Herrada, M.; Gañán-Calvo, A.M.; Montanero, J. Effect of an axial electric field on the breakup of a leaky-dielectric liquid filament. *Phys. Fluids* **2021**, *33*, 092114. [[CrossRef](#)]
26. Vagner, S.; Patlazhan, S.; Serra, C.; Funfschilling, D.; Kulichikhin, V. Dripping and jetting of semi-dilute polymer solutions co-flowing in co-axial capillaries. *Phys. Fluids* **2021**, *33*, 062002. [[CrossRef](#)]
27. Liu, S.; Liang, G.; Li, C.; Zhang, L.; Che, J.; Shen, S. The falling, necking, and break-up of droplet between horizontal tubes with low Reynolds number. *Int. J. Multiph. Flow* **2021**, *142*, 103717. [[CrossRef](#)]
28. Yu, X.; Wu, Y.; Li, Y.; Yang, Z.; Ma, Y. The formation of satellite droplets in micro-devices due to the rupture of neck filament. *Chem. Eng. Res. Des.* **2020**, *153*, 435–442. [[CrossRef](#)]
29. Broboana, D.; Bratu, A.M.; Magos, I.; Patrascu, C.; Balan, C. Kinematics of the viscous filament during the droplet breakup in air. *Sci. Rep.* **2022**, *12*, 1774. [[CrossRef](#)]
30. Weickgenannt, C.; Roisman, I.V.; Tropea, C. Pinch-off of a stretching viscous filament and drop transport. *New J. Phys.* **2015**, *17*, 083059. [[CrossRef](#)]
31. Pedregosa, F.; Varoquaux, G.; Gramfort, A.; Michel, V.; Thirion, B.; Grisel, O.; Blondel, M.; Prettenhofer, P.; Weiss, R.; Dubourg, V.; et al. Scikit-learn: Machine learning in Python. *J. Mach. Learn. Res.* **2011**, *12*, 2825–2830.
32. Sadat, T. A comparative study of machine learning approaches for predicting viscosity in Sacran/CNF solutions. *Chem. Phys. Lett.* **2024**, *836*, 141022. [[CrossRef](#)]
33. Breiman, L. Random forests. *Mach. Learn.* **2001**, *45*, 5–32. [[CrossRef](#)]
34. Shafiq, M.; Gu, Z. Deep residual learning for image recognition: A survey. *Appl. Sci.* **2022**, *12*, 8972. [[CrossRef](#)]
35. Basaran, O.A. Small-scale free surface flows with breakup: Drop formation and emerging applications. *Am. Inst. Chem. Eng. AIChE J.* **2002**, *48*, 1842. [[CrossRef](#)]
36. Hadavimoghaddam, F.; Ostadhassan, M.; Heidaryan, E.; Sadri, M.A.; Chapanova, I.; Popov, E.; Cheremisin, A.; Rafieepour, S. Prediction of dead oil viscosity: Machine learning vs. classical correlations. *Energies* **2021**, *14*, 930. [[CrossRef](#)]

**Disclaimer/Publisher’s Note:** The statements, opinions and data contained in all publications are solely those of the individual author(s) and contributor(s) and not of MDPI and/or the editor(s). MDPI and/or the editor(s) disclaim responsibility for any injury to people or property resulting from any ideas, methods, instructions or products referred to in the content.